

Determining the optical and polaritonic properties of isotopically pure hBN using cryogenic FTIR micro-spectroscopy

Siddharth Nandanwar^{1,2}, Aditya Desai¹, S. Maryam Vaghefi Esfidani¹, Tristan McMillan¹, Eli Janzen³, James H. Edgar³, and Thomas G. Folland^{1*}

¹ Department of Physics and Astronomy, The University of Iowa, Iowa City, Iowa, 52245

² Department of Physics, Boston College, Chestnut Hill, Massachusetts 02467, USA

³ Tim Taylor Department of Chemical Engineering, Durland Hall, Kansas State University, Manhattan, KS 66506

*thomas-folland@uiowa.edu

Abstract

Van-der-Waals materials support numerous exotic polaritonic phenomena originating from their layered structures and associated vibrational and electronic properties. However, many van-der-Waals materials' unique properties are most prominent at cryogenic temperatures. This presents a particular challenge for polaritonics research, as reliable optical constant data is required for understanding light-matter coupling. This paper presents a cryogenic Fourier transform infrared microscope design constructed entirely from off-the-shelf components and fitting procedures for determining optical constants in the infrared. Data correction techniques were developed to directly quantify systematic errors in the fitting procedure. We use this microscope to present the first temperature-dependent characterization of the optical properties of hexagonal boron nitride enriched with isotopically pure boron. Our full analysis of the infrared dielectric function shows small but significant tuning of the optical constants, which is highly consistent with Raman data from the literature. We then use this dielectric data to perform and analyze the polariton propagation properties, which agree exceptionally well with published cryogenic scattering-type nearfield microscopy results. In addition to the insights gained into hyperbolic polaritons in hBN, our paper represents a transferable framework for characterizing exfoliated infrared polaritonic materials and other infrared devices. This could accelerate discoveries in

different material systems, especially those that are spatially inhomogeneous or cannot be prepared as large single crystals.

Main Body

In recent years, research into mid- and far-infrared (3-100 μ m) polaritonics has rapidly expanded owing to the emergent physical phenomena in this wavelength range¹. One growth area has been the study of van-der-Waals (vdW) materials^{2,3}, with a layered structure that leads to effects including hyperbolicity⁴⁻⁷ and ballistic transport⁸. They are prepared from bulk crystal samples through exfoliation, producing high-quality thin films on arbitrary substrates⁹. Many properties of vdW materials including phase transitions¹⁰, high mobility behavior^{8,11}, carrier freeze-out¹², and damping pathways¹³, cannot be studied at room temperature. These effects are essential for emerging quantum technologies¹⁴, in which polaritonics play a crucial role¹⁵. Therefore, developing techniques for studying infrared polaritonics in vdW crystallites at low temperatures is critical.

One approach to measuring polaritons in vdW materials is near-field microscopy, which exploits a sharp metal probe to get a precise spatial resolution (10nm) at a wide range of wavelengths from the infrared to THz¹⁶. However, the reliance on laser sources, the restricted sensitivity to polarization¹⁷, and the possibility of artifacts in the data¹⁸, make it less versatile for general-purpose characterization or materials screening. Far-field techniques are diffraction-limited but make up for spatial resolution by offering excellent spectral bandwidth and polarization control, which can span the entire mid-infrared^{1,19}. FTIR microscopy is the primary route to achieving this and can measure individual van-der-Waals flakes²⁰. Several approaches to FTIR micro cryo-spectroscopy for small samples have been developed in past works^{11,21-27}. Parabolic focusing on sub-mm crystallites and subsequent gold overcoating for referencing²⁸ can measure relatively large crystals^{22,29,30}. However, it is unsuited for single, exfoliated flake analysis with a size of 100 μ m or less. Transmission-based focusing setups leveraging light pipes are also effective on this length scale^{26,27}. However, these cannot perform reflection-based spectroscopy, and are not suited to mapping. Finally, several groups have adapted a commercial He cryostat to a commercial FTIR microscope and have been used to study van-der Waals materials^{11,21,24,31}. However, commercial microscope systems often cannot be adapted for advanced infrared microscopy techniques. The fixed geometry limits the range of cryostats that can be used and the

optical components that can be inserted into the beam path for advanced polarimetry or optical pumping experiments. Commercial systems also use extensive custom optics, which makes it challenging to reproduce their designs accurately in the laboratory and repairs require service visits. Finally, the costs associated with commercial microscope components can be significant.

This paper presents the design for an infrared cryo-microscope that leverages off-the-shelf components capable of performing precision reflection and dielectric function measurements. Our approach can be applied to any combination of FTIR and cryostat and can be optimized for polarimetry and other experiments. We study the temperature dependent optical properties of ^{10}B and ^{11}B enriched hexagonal boron nitride. These materials have record-breaking propagation lengths for hyperbolic phonon polaritons (HPhPs), owing to the reduced scattering in isotopically pure materials^{13,18,32–34}. Both $h^{10}\text{BN}$ and $h^{11}\text{BN}$ have been shown to have extended polariton lifetime at low temperatures^{13,35}; however, the full dielectric function is not available. While such information is available for hBN with naturally distributed boron isotopes²², the damping parameters and phonon tuning of isotopically pure materials is not available. First, we examine samples prepared on an Au mirror, which has strong background reflectance from the substrate that aids in referencing. We observe Fabry-Perot (FP) type absorption resonances^{36,37} in the mid-IR, which is well suited to determining the temperature dependence of TO phonons in the infrared. We also use sapphire substrates, which are better suited for completing a full dielectric function analysis close to both TO and LO phonon energies. Our dielectric function analysis extends previous methods^{7,20} implementing a method for backside reflection correction, and addressing systematic errors. We find that optical losses in isotopically pure hBN at room temperature were previously underestimated by a factor of 2. This parameter is critical for realistic simulations of polariton propagation in hBN materials and heterostructures. Our results are consistent with past measurements on Raman modes¹³, and hBN polaritons for which no model previously existed³⁵. Our results for the dielectric function show comparable shifts in the TO phonon energy as the FP resonances, suggesting that tracking the properties of FP modes is a suitable mechanism for estimating the temperature dependence of phonon properties. Finally, we calculate the quality factors of polaritons as a function of temperature and show that our temperature-dependent dielectric function closely matches prior experiments by Ni³⁵. This suggests our dielectric function improves on those previously published, even at room temperature, and can be used for predictive modeling for polaritonic devices.

Our microscope implements a conventional, finite conjugate length optical microscope using all-reflective optical components, with a schematic shown in **Fig. 1a**. Indicative full beam power spectra are shown in **Fig 1b**, comparing the spectra from the microscope with a 3mm aperture (measured 60 μ m spot size) to a conventional configuration FTIR (SiC Glow Bar, KBr beam-splitter, and DLaTGS detector). For more details, please see the **Supplemental Section 1**. Temperature-dependent micro-FTIR spectra of a flake of boron h¹⁰BN, which is 1220nm thick, exfoliated onto an Au-coated silicon substrates substrate at 300K and 5K are shown in **Fig. 2a**. There are resonances are observed in the spectral ranges of approximately 840cm⁻¹ and from 1200-1400cm⁻¹. We attribute these to a Fabry Perot-type resonance associated with the high index of the h¹⁰BN close to the TO phonon (located at 1393cm⁻¹), which is reported to exceed 25 in prior works³². These have been reported previously in the context of FTIR-ATR measurements³⁶, on bulk³⁸, and on exfoliated flakes^{37,34}. The out-of-plane resonances can be measured due to the reflective objective's off-normal incidence angle. The narrow spikes in the range of 1400-1800cm⁻¹ can be attributed to atmospheric water absorption.

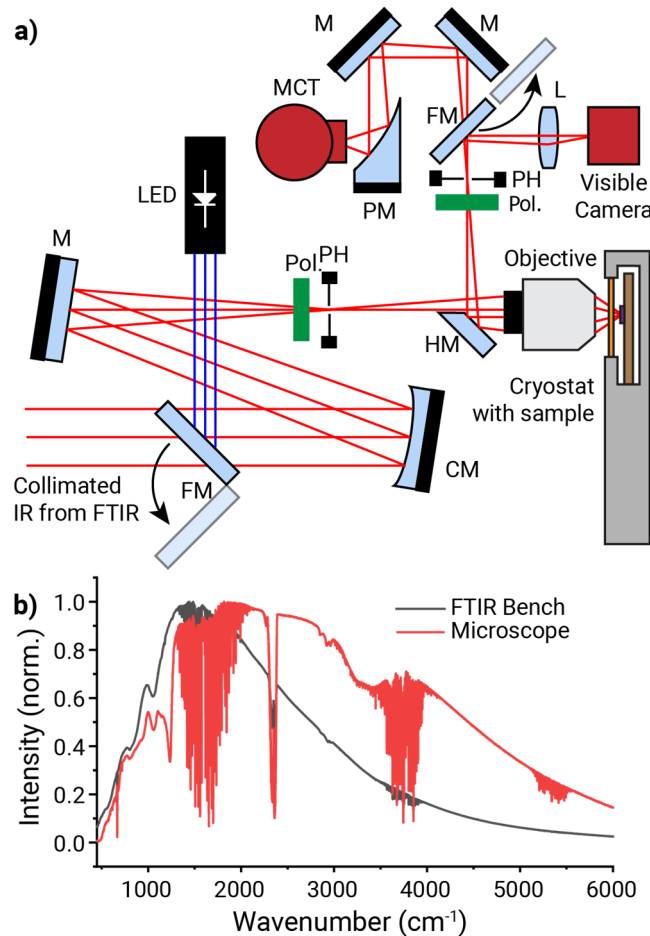


Figure 1. Schematic of the FTIR cryo-microscopy setup. a) shows the optical configuration, with abbreviations M-mirror, CM – Concave mirror, PM – parabolic mirror, HM-Half mirror, FM – flip mirror, L- lens, LED – light emitting diode, Pol. – Polarizer and PH – Pinhole b) compares the comparative spectral throughput of our system against the FTIR bench.

A detailed view of the resonance associated with the out-of-plane phonon and the lower Reststrahlen band of $h^{10}\text{BN}$ is shown in **Fig. 2b**. The linewidth is sharp, consistent with the long lifetime of the out-of-plane phonon³², and shows almost no temperature dependence. The resonances associated with the high energy phonon is also presented in **Fig. 2c**. A series of resonances in the spectra are present, with varying absorption strength and linewidth as they approach the TO phonon located at approximately 1393cm^{-1} . First, we consider the resonance frequency of these modes - they redshift with increasing temperature, with a tuning range of $1.8\pm 0.1\text{cm}^{-1}$, $2.7\text{cm}^{-1}\pm 0.1$ and $2.5\pm 0.1\text{cm}^{-1}$, for modes FP1, FP2, and FP3 respectively. This is suggestive of temperature tuning of the TO phonon in $h\text{BN}$. The trend in linewidth between the

modes is more subtle. The linewidth of FP resonances is related to a combination of material and radiative damping. As the refractive index increases close to the TO phonon, radiative damping decreases due to increased reflection at the interface between hBN and air. Meanwhile, light more readily gets absorbed by the TO phonon, so material absorption rises dramatically. This makes resonances sharper as they approach the TO phonon as the radiative losses decrease but then get significantly broader once the TO phonon losses increase. A more detailed discussion of modal lifetime for standing wave resonances can be found in prior work³⁹. There is a slight change in the model linewidth with temperature - taking FP3 as an example, we can see that the full-width half maximum changes from 3.2 cm^{-1} to 3.7 cm^{-1} between 5K and 300K, suggesting a small but notable change in the mode lifetime.

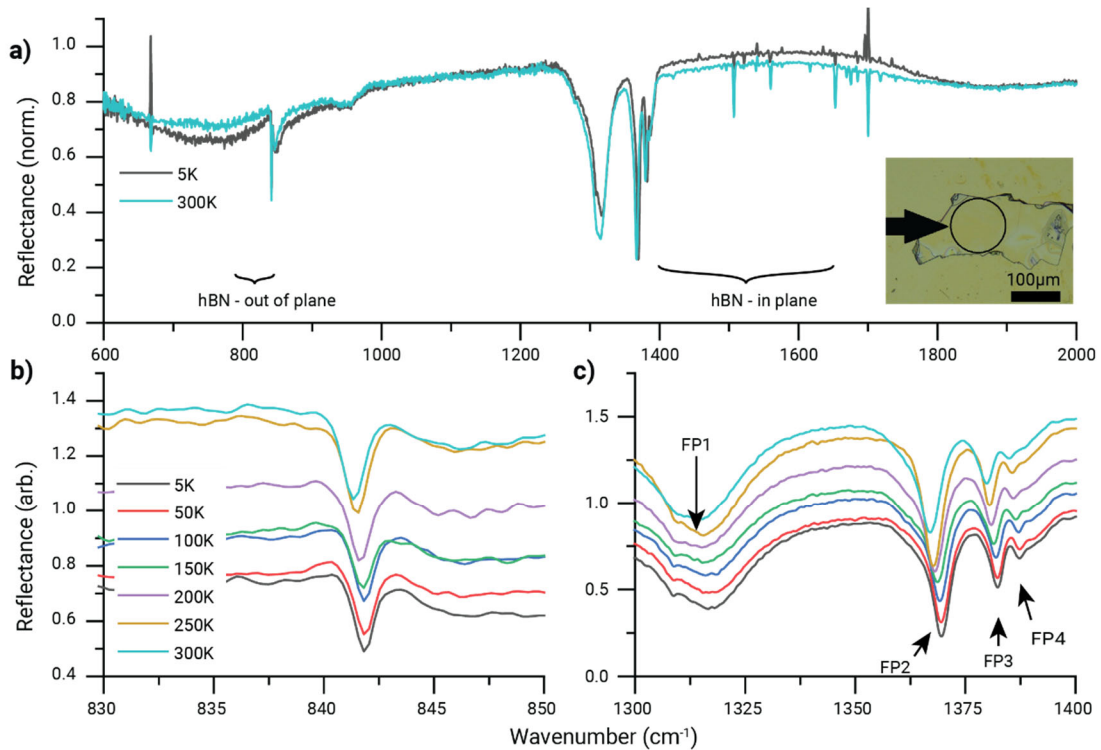


Figure 2. Temperature-dependent infrared spectra of $h^{10}\text{BN}$ on Au/Ti coated silicon substrates. **a)** shows broadband reflectance spectra, **b)** shows resonances associated with the out-of-plane phonon **c)** shows resonances associated with the in-plane phonon. Inset shows an optical image of the flake.

These results are compared with temperature dependent micro-FTIR spectra of a flake of boron $h\text{B}^{10}\text{N}$ with 700nm thickness exfoliated onto a sapphire substrate, as shown in **Fig. 3a**. We see

several spectral features across the mid-infrared, including the phonon response of the sapphire substrate (900cm^{-1} and below), a sharp dip associated with the out of plane phonon of hBN at approximately 842cm^{-1} , and the in-plane Reststrahlen band from approximately 1395cm^{-1} to 1650cm^{-1} . The resonance associated with the out-of-plane phonon of h^{10}BN can be seen in the Reststrahlen band of sapphire, as shown in **Fig 3b**, similar to the results on Au. In the hBN upper Reststrahlen band, **Fig 3c**. Each mode redshifts with increasing temperature, with the mode labeled FP1 tuning $2.5\pm 0.5\text{cm}^{-1}$ and FP2 tuning $2.6\pm 0.1\text{cm}^{-1}$. These can be directly contrasted with the results for FP3 on Au, which shows $2.5\pm 0.1\text{cm}^{-1}$ of tuning. Similarly, the linewidth slightly broadens with temperature, going from $6.8\pm 0.3\text{cm}^{-1}$ to $7.3\pm 0.3\text{cm}^{-1}$. This consistency between substrates suggests a phonon tuning of approximately 2.5cm^{-1} , and a reduction of the phonon lifetime. Similar results are seen for a flake of isotopically pure h^{11}BN and a second thinner flake of h^{10}BN , detailed in **Supplemental Section 2**.

To determine the optical constants of the hBN, we use a commercial piece of software WAVSE from J. A. Wollam, and homebuilt. a nonlinear least squares fitting algorithm based on a 4×4 transfer matrix formalism published in ⁴⁰, with both giving consistent results. Details of the fitting procedure are presented in **Supplemental Section 3**. Spectral fits for the reflectance spectrum at 5K are shown in **Fig 4a/b**. There is an excellent agreement between the modeled results and experimentally measured reflectance spectra around the TO phonon. The deviation above the Reststrahlen band is attributed to reflections off the backside of the substrate, partially compensated in our fitting procedure. We conducted analysis for two h^{10}BN flakes and one h^{11}BN enriched flake, fitting spectra for temperatures between 5.5 and 300K. Fits are shown in **Supplemental Section 4**.

The temperature-dependent parameters for ω_{TO} and Γ are shown in **Fig 4c-d**, for both isotopes . The phonon energy continuously redshifts with increasing temperature for all flakes studied here, consistent with prior Raman studies by Cuscó. Through the deviations between the two parameters, we can estimate systematic errors at 0.9cm^{-1} , as discussed in more detail in **SI section 6**. We highlight that our results show a slightly lower room temperature phonon energy than that previously reported in the literature by Giles³², likely attributed to the lower resolution of prior measurements at 2cm^{-1} . The tuning of the extracted TO phonon is consistent with that of the FP modes, demonstrating that FP mode tuning can provide the tuning of the TO phonon. The

trends observed for the phonon energy with temperature can be described by a combination of lattice contraction (increasing phonon energy) and phonon anharmonic interaction (decreasing phonon energy). For many semiconductors, this has led to an overall redshift with a temperature of a few wavenumbers. This contrasts with recent work on MoO₃, with an overall phonon blueshift³¹. The differences between hBN and MoO₃ are likely associated with weak anharmonicity in the MoO₃ suppressing higher-order anharmonic perturbations to the phonons, giving a predominantly lattice contraction-induced blueshift of the phonon.

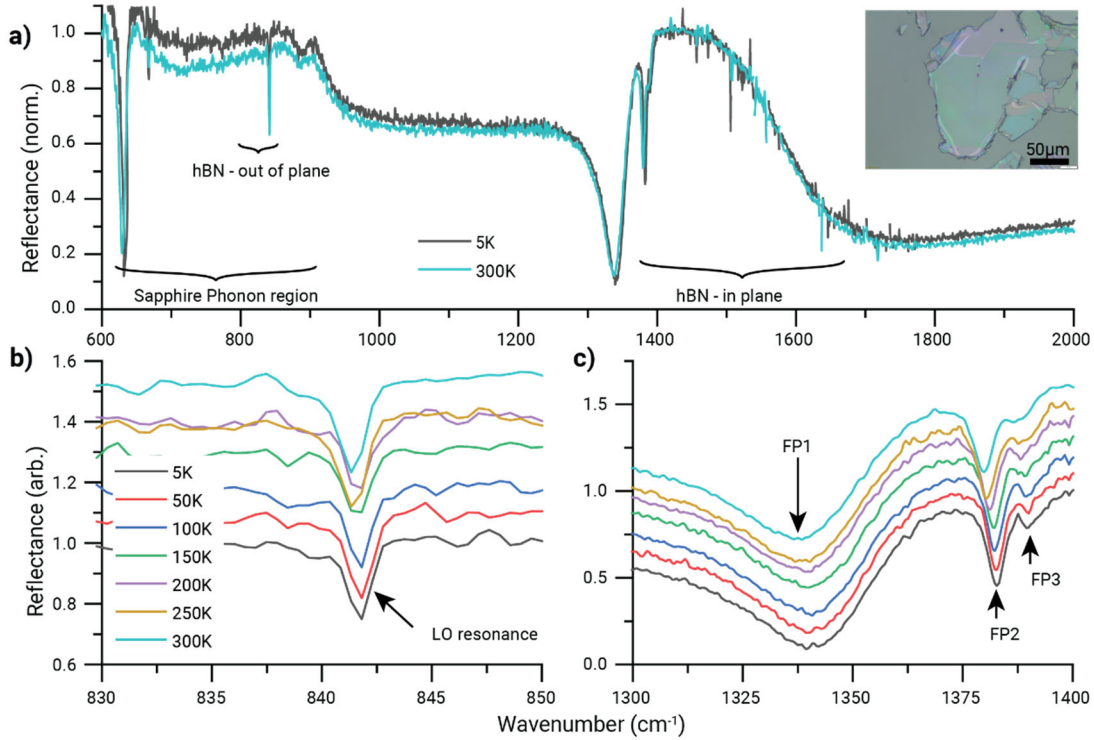


*Figure 3. Temperature-dependent infrared spectra of h^{10} BN on Sapphire substrates. **a)** shows broadband reflectance spectra, **b)** shows resonance associated with the out-of-plane phonon **c)** shows resonances associated with the in-plane phonon. Inset shows an optical image of the flake.*

Our results for damping Γ are shown in **Fig 4d-e** are also consistent with recent Raman and s-SNOM studies, showing that the phonon linewidths are reduced as the samples are cooled. Our results for damping are significantly larger than those reported in Giles³². We can attribute this to the harmonic model used in Giles³² where an anharmonic model is more applicable²³. As discussed in SI section 6 we estimate systematic errors during the fit of 0.47cm^{-1} . To better

compare our results with those from Ni³⁵, we use the temperature-dependent fitting function proposed in that work;

$$\gamma(T) = \gamma_0 \left(1 + \frac{8\pi^2}{15} \frac{T^4}{T_\lambda^4} \right) \quad (2)$$

Where T is the temperature, γ_0 is the low-temperature damping limit, and T_λ is the characteristic temperature. Fitting to Figure 4, we get a characteristic temperature of 1200 ± 100 K for the 700 nm h¹⁰BN flake, 1110 ± 60 K for the 500 nm thick h¹⁰BN flake and 1060 ± 30 K for the 750 nm thick h¹¹BN flake. These consistent values support the hypothesis that the damping is given mainly by acoustic phonon scattering. While this value is approximately twice the value presented by Ni³⁵, this is likely due to uncertainties in extracted parameters. Finally, the change in the line widths of the FP modes in the reflectance spectrum on Au or Sapphire gives a comparable shift to that of the damping extracted from dielectric function analysis. As such, we believe that fitting the line shape of FP modes close to the TO phonon can approximate the temperature-dependent properties of ω_{TO} and Γ . The framework for the dependence presented in equation 2 is a phenomenological model that considers the population of acoustic phonons. This T⁴ dependence will be general for any material with sufficiently high acoustic phonon energies to be the dominant scattering term, where isotopic impurities are insignificant. This dependence would, therefore, be anticipated to hold for other high phonon energy materials, such as silicon carbide, cBN, and AlN.

While our results for ω_{TO} and Γ are in general agreement with prior literature and extend the previously reported values, we find that both ω_{LO} and ϵ_∞ parameters show some inconsistencies which prevents observation of temperature trends. (See **Supplementary Section 5**). While this is a limitation of our approach, we show in **Supplementary Section 7** that our dielectric function can reproduce the FP mode tuning from the flake in Figure 2, suggesting that our model is accurate enough for predictive modeling.

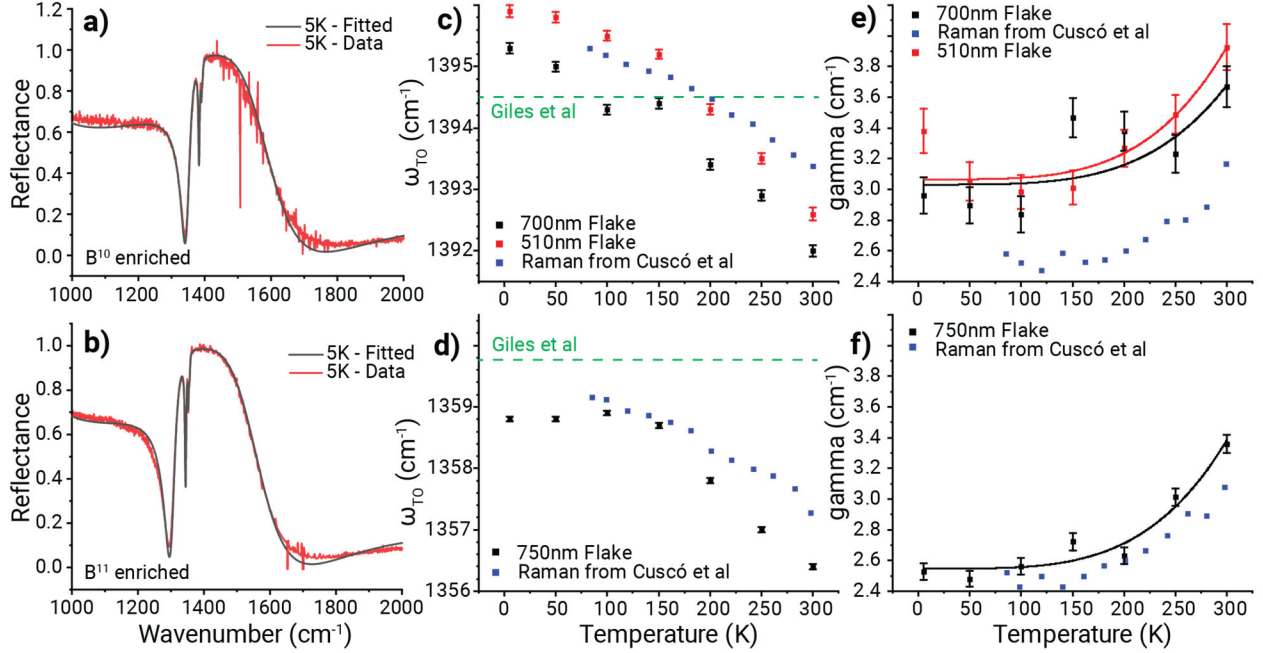


Figure 4. Dielectric function extraction from hBN flake reflectance spectra **a)/b)** shows fitted spectrum for a 700nm thick h^{10} BN and h^{11} BN enriched flake respectively **c)/d)** shows experimentally extracted TO phonon values for h^{10} BN and h^{11} BN respectively **e)/f)** shows experimentally extracted phonon damping values h^{10} BN and h^{11} BN, respectively.

Finally, we assess the properties of the hyperbolic phonon polaritons in hexagonal boron nitride. The expression gives the dispersion of hyperbolic polaritons in the high k limit⁴;

$$kd = (k' + ik'')d = -\psi \left[\text{atan} \left(\frac{\epsilon_o}{\epsilon_t \psi} \right) + \text{atan} \left(\frac{\epsilon_s}{\epsilon_t \psi} \right) + \pi l \right], \quad \psi = -i \sqrt{\frac{\epsilon_z}{\epsilon_t}} \quad (3)$$

Where d is the flake thickness, ϵ_o is the dielectric function above the hBN flake, ϵ_s is the dielectric function of the substrate, ϵ_t is the in-plane dielectric function, ϵ_z is the out-of-plane dielectric function, and l is an integer, set to 1 here. We examine the polariton dispersion (k'), and the mode Q factor (k'/k'') as shown in **Fig. 5a/b)**. We only consider the extreme cases of 300K and 5K and calculate for both suspended hBN and on SiO_2 . The dispersion only changes slightly between room temperature and 5K. However, the mode quality factors show a dramatic change in behavior. The reduction in the losses at low-temperature results in a quality factor approximately 30% larger than at room temperature in the center of the Reststrahlen band for suspended flakes. This enhancement is reduced on SiO_2 substrates, suggesting that the losses in

SiO₂ suppress the benefits of cryogenic cooling. We can compare our results against quality factor values taken from Ni³⁵, and we show excellent agreement between our modeled values and prior experiments. These represent the closest agreement between s-SNOM and far-field studies reported for isotopically pure hBN, suggesting that our higher damping values than those of Giles³² represent the actual loss in isotopically pure hBN.

To further explore the correlation between far-field and near-field measurements, we also calculate the polariton damping factor, which can be evaluated from³⁵ $\gamma(T) = \omega v_g / (Q(T) v_p)$, where v_g and v_p are the group and phase velocities of the polariton, respectively. Both v_p and v_g are evaluated from the dispersion in Fig 5a, with $\gamma(T)$ shown in **Fig 5c**. Our results for suspended h¹¹BN are consistent with the published data, which accounts for substrate losses. We can also evaluate the damping associated with the SiO₂, which is shown to be 0.2cm⁻¹ at a frequency of 1522cm⁻¹. Fitting to equation 2, we find a characteristic temperature $T_\lambda = 1060 \pm 30\text{K}$ identical to the phonon value. This suggests that the previously reported damping associated with hyperbolic phonon polaritons in boron nitride is almost entirely given by losses to the phonon part of the polariton. Based on polariton imaging alone, this is impossible to determine, demonstrating the complementary nature of near- and far-field measurements. In addition to the polariton wave-vector and Q factor, in the supplementary information figure S8, we present polariton group velocity (v_g), propagation length ($L_p = 1/2k''$), and lifetime ($\tau = L_p/v_g$) at room and low temperature. Our values for the dielectric function are determined for low momentum and omit non-locality predicted at extremely high phonon polariton momenta (ref⁴¹).

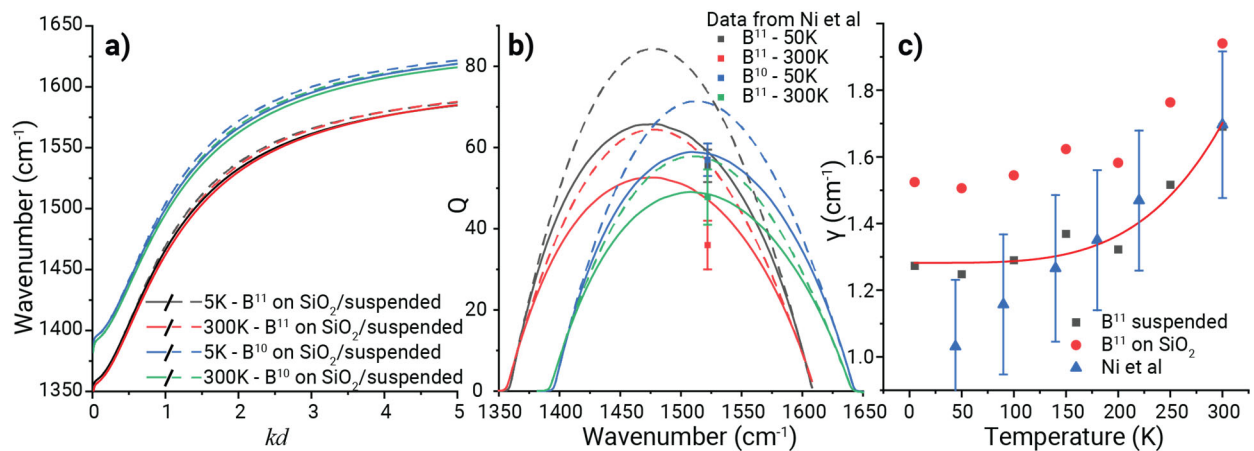


Figure 5. Polariton dispersion and lifetime extracted from measured dielectric functions a) shows polariton dispersion for $h^{10}\text{BN}$ and $h^{11}\text{BN}$ on a SiO_2 substrate and suspended in air. b) shows the mode Q factor, defined as k'/k'' , for $h^{10}\text{BN}$ and $h^{11}\text{BN}$ on both a SiO_2 substrate and suspended, compared against data from Ni^{35} . c) shows polariton damping rate and a temperature-dependent fit from our dielectric function, again compared against Ni^{35} for $h\text{B}^{11}\text{N}$.

In this paper, we have detailed a design of a cryogenic FTIR microscope constructed using off-the-shelf components capable of measuring the infrared optical properties of exfoliated van-der-Waals materials. We measure the temperature-dependent properties of ^{10}B and ^{11}B isotopically pure hBN, evaluated the full infrared dielectric function as a function of temperature. Our results are consistent with past Raman and polaritonic studies and suggest that the polariton losses at room temperature have been significantly underestimated in prior works. This allows us to explain experimentally measured properties of HPhPs at low temperatures and generalize prior results to the full Reststrahlen band. Our work and methods can be applied beyond hBN to a much more comprehensive set of van der Waals materials, including those with phase transitions, free electron plasmas, and other optical phenomena.

Acknowledgments

SN, TM, and AD acknowledge funding through the University of Iowa Office for Undergraduate Research. TGF acknowledges funding from NSF Grant 2318049, ‘Phonon Polariton Based Infrared Optoelectronics’ and ONR Grant N00014-23-1-2616, ‘Ultrafast, nano-optic and temperature-dependent infrared (IR) probes for wide bandgap semiconductor characterization’. SMVE acknowledges funding through NSF grant Grant 2318049, ‘Phonon Polariton Based Infrared Optoelectronics’, as well as the University of Iowa Startup funding. ONR award N00014-22-1-2582 provided EJ and JHE support for hBN crystal growth

References

- (1) Folland, T. G.; Nordin, L.; Wasserman, D.; Caldwell, J. D. D. Probing Polaritons in the Mid- to Far-Infrared. *J Appl Phys* **2019**, *125* (19), 191102. <https://doi.org/10.1063/1.5090777>.
- (2) Geim, A. K.; Grigorieva, I. V. Van Der Waals Heterostructures. *Nature* **2013**, *499*, 419–425.
- (3) Kim, S.; Menabde, S. G.; Brar, V. W.; Jang, M. S. Functional Mid-Infrared Polaritonics in van Der Waals Crystals. *Adv Opt Mater* **2020**, *8* (5), 1901194. <https://doi.org/https://doi.org/10.1002/adom.201901194>.
- (4) Dai, S.; Fei, Z.; Ma, Q.; Rodin, A. S.; Wagner, M.; McLeod, A. S.; Liu, M. K.; Gannett, W.; Regan, W.; Thiemens, M.; Dominguez, G.; Castro Neto, A. H.; Zettl, A.; Keilmann, F.; Jarillo-Herrero, P.; Fogler, M. M.; Basov, D. N. Tunable Phonon Polaritons in Atomically Thin van Der Waals Crystals of Boron Nitride. *Science (Washington)* **2014**, *343* (6175), 1125–1129.
- (5) Zheng, Z.; Xu, N.; Oscurato, S. L.; Tamagnone, M.; Sun, F.; Jiang, Y.; Ke, Y.; Chen, J.; Huang, W.; Wilson, W. L.; Ambrosio, A.; Deng, S.; Chen, H. A Mid-Infrared Biaxial Hyperbolic van Der Waals Crystal. *Sci Adv* **2019**, *5* (5), eaav8690. <https://doi.org/10.1126/sciadv.aav8690>.
- (6) Ma, W.; Alonso-González, P.; Li, S.; Nikitin, A. Y.; Yuan, J.; Martín-Sánchez, J.; Taboada-Gutiérrez, J.; Amenabar, I.; Li, P.; Vélez, S.; Tollan, C.; Dai, Z.; Zhang, Y.; Sriram, S.; Kalantar-Zadeh, K.; Lee, S.-T.; Hillenbrand, R.; Bao, Q. In-Plane Anisotropic and Ultra-Low-Loss Polaritons in a Natural van Der Waals Crystal. *Nature* **2018**, *562* (7728), 557–562. <https://doi.org/10.1038/s41586-018-0618-9>.
- (7) Caldwell, J. D.; Kretinin, A. V.; Chen, Y.; Giannini, V.; Fogler, M. M.; Francescato, Y.; Ellis, C. T.; Tischler, J. G.; Woods, C. R.; Giles, A. J.; Hong, M.; Watanabe, K.; Taniguchi, T.; Maier, S. A.; Novoselov, K. S. Sub-Diffractive, Volume-Confined Polaritons in the Natural Hyperbolic Material Hexagonal Boron Nitride. *Nat Commun* **2014**, *5*, 5221. <https://doi.org/10.1038/ncomms6221>.
- (8) Ni, G. X.; McLeod, A. S.; Sun, Z.; Wang, L.; Xiong, L.; Post, K. W.; Sunku, S. S.; Jiang, B. Y.; Hone, J.; Dean, C. R.; Fogler, M. M.; Basov, D. N. Fundamental Limits to Graphene Plasmonics. *Nature* **2018**, *557* (7706), 530–533. <https://doi.org/10.1038/s41586-018-0136-9>.
- (9) Fan, S.; Vu, Q. A.; Tran, M. D.; Adhikari, S.; Lee, Y. H. Transfer Assembly for Two-Dimensional van Der Waals Heterostructures. *2d Mater* **2020**, *7* (2), 22005. <https://doi.org/10.1088/2053-1583/ab7629>.
- (10) Frenzel, A. J.; McLeod, A. S.; Wang, D. Z. R.; Liu, Y.; Lu, W.; Ni, G.; Tsen, A. W.; Sun, Y.; Pasupathy, A. N.; Basov, D. N. Infrared Nanoimaging of the Metal-Insulator

- Transition in the Charge-Density-Wave van Der Waals Material 1T-TaS₂. *Phys Rev B* **2018**, *97* (3), 1–7. <https://doi.org/10.1103/PhysRevB.97.035111>.
- (11) Xie, Y.; Wang, C.; Fei, F.; Li, Y.; Xing, Q.; Huang, S.; Lei, Y.; Zhang, J.; Mu, L.; Dai, Y.; Song, F.; Yan, H. Tunable Optical Topological Transitions of Plasmon Polaritons in WTe₂ van Der Waals Films. *Light Sci Appl* **2023**, *12* (1), 193. <https://doi.org/10.1038/s41377-023-01244-w>.
 - (12) Srivastava, S.; Mohapatra, Y. N. MoS₂/ZnO Isotype Heterostructure Diode: Carrier Transport and Band Alignment. *J Appl Phys* **2021**, *129* (20). <https://doi.org/10.1063/5.0048592>.
 - (13) Cuscó, R.; Edgar, J. H.; Liu, S.; Li, J.; Artús, L. Isotopic Disorder: The Prevailing Mechanism in Limiting the Phonon Lifetime in Hexagonal BN. *Phys Rev Lett* **2020**, *124* (16). <https://doi.org/10.1103/PhysRevLett.124.167402>.
 - (14) Basov, D. N.; Averitt, R. D.; Hsieh, D. Towards Properties on Demand in Quantum Materials. *Nat Mater* **2017**, *16* (11), 1077–1088. <https://doi.org/10.1038/NMAT5017>.
 - (15) Liew, T. C. H. The Future of Quantum in Polariton Systems: Opinion. *Opt Mater Express* **2023**, *13* (7), 1938–1946. <https://doi.org/10.1364/OME.492503>.
 - (16) Kwon, S.; Kim, J. M.; Ma, P. J.; Guan, W.; Nam, S. Near-Field Nano-Optical Imaging of van Der Waals Materials. *Advanced Physics Research* **2023**, *2* (10), 2300009. <https://doi.org/https://doi.org/10.1002/apxr.202300009>.
 - (17) Kaps, F. G.; Kehr, S. C.; Eng, L. M. Polarization Sensitivity in Scattering-Type Scanning Near-Field Optical Microscopy—Towards Nanoellipsometry. *Applied Sciences (Switzerland)* **2023**, *13* (18). <https://doi.org/10.3390/app131810429>.
 - (18) Pavlidis, G.; Schwartz, J. J.; Matson, J.; Folland, T.; Liu, S.; Edgar, J. H.; Caldwell, J. D.; Centrone, A. Experimental Confirmation of Long Hyperbolic Polariton Lifetimes in Monoisotopic (10B) Hexagonal Boron Nitride at Room Temperature. *APL Mater* **2021**, *9* (9), 91109. <https://doi.org/10.1063/5.0061941>.
 - (19) Griffiths, P. R. *Fourier Transform Infrared Spectrometry*, 2nd Ed.; De Haseth, J. A., Ed.; Wiley-Interscience: Hoboken, N.J., 2007.
 - (20) Álvarez-Pérez, G.; Folland, T. G.; Errea, I.; Taboada-Gutiérrez, J.; Duan, J.; Martín-Sánchez, J.; Tresguerres-Mata, A. I. F.; Matson, J. R.; Bylinkin, A.; He, M.; Ma, W.; Bao, Q.; Martín, J. I.; Caldwell, J. D.; Nikitin, A. Y.; Alonso-González, P. Infrared Permittivity of the Biaxial van Der Waals Semiconductor A-MoO₃ from Near- and Far-Field Correlative Studies. *Advanced Materials* **2020**, *32* (29), 1908176. <https://doi.org/10.1002/adma.201908176>.
 - (21) Wang, C.; Huang, S.; Xing, Q.; Xie, Y.; Song, C.; Wang, F.; Yan, H. Van Der Waals Thin Films of WTe₂ for Natural Hyperbolic Plasmonic Surfaces. *Nat Commun* **2020**, *11* (1), 1158. <https://doi.org/10.1038/s41467-020-15001-9>.

- (22) Homes, C. C.; Ali, M. N.; Cava, R. J. Optical Properties of the Perfectly Compensated Semimetal WTe₂. *Phys Rev B Condens Matter Mater Phys* **2015**, *92* (16). <https://doi.org/10.1103/PhysRevB.92.161109>.
- (23) Segura, A.; Cuscó, R.; Taniguchi, T.; Watanabe, K.; Artús, L. Long Lifetime of the E_{1u} In-Plane Infrared-Active Modes of h-BN. *Phys Rev B* **2020**, *101* (23). <https://doi.org/10.1103/PhysRevB.101.235203>.
- (24) Nedoliuk, I. O.; Hu, S.; Geim, A. K.; Kuzmenko, A. B. Colossal Infrared and Terahertz Magneto-Optical Activity in a Two-Dimensional Dirac Material. *Nat Nanotechnol* **2019**, *14* (8), 756–761. <https://doi.org/10.1038/s41565-019-0489-8>.
- (25) Crassee, I.; Orlita, M.; Potemski, M.; Walter, A. L.; Ostler, M.; Seyller, T.; Gaponenko, I.; Chen, J.; Kuzmenko, A. B. Intrinsic Terahertz Plasmons and Magnetoplasmons in Large Scale Monolayer Graphene. *Nano Lett* **2012**, *12*, 2470–2474. <https://doi.org/10.1021/nl300572y> LB - Graphene;Static Plasmons.
- (26) Midlíková, J. D.; Šedivý, M.; Sojka, A.; Santana, V. T.; Dubroka, A.; Neugebauer, P. A Versatile Setup for Fourier-Transform Infrared Magneto-Spectroscopy. *IEEE Trans Instrum Meas* **2023**, *72*, 1–11. <https://doi.org/10.1109/TIM.2023.3284943>.
- (27) Jiang, Z.; Henriksen, E. A.; Tung, L. C.; Wang, Y.-J.; Schwartz, M. E.; Han, M. Y.; Kim, P.; Stormer, H. L. Infrared Spectroscopy of Landau Levels of Graphene. *Phys Rev Lett* **2007**, *98* (19), 197403. <https://doi.org/10.1103/PhysRevLett.98.197403>.
- (28) Homes, C. C.; Reedyk, M.; Cradles, D. A.; Timusk, T. Technique for Measuring the Reflectance of Irregular, Submillimeter-Sized Samples. *Appl Opt* **1993**, *32* (16), 2976–2983. <https://doi.org/10.1364/AO.32.002976>.
- (29) Barker, A. S.; Ditzenberger, J. A.; DiSalvo, F. J. Infrared Study of the Electronic Instabilities in Tantalum Disulfide and Tantalum Diselenide. *Phys Rev B* **1975**, *12* (6), 2049–2054. <https://doi.org/10.1103/PhysRevB.12.2049>.
- (30) Dutta, U.; Sahoo, S.; Malavi, P. S.; Piccirilli, F.; Di Pietro, P.; Perucchi, A.; Lupi, S.; Karmakar, S. Infrared Spectroscopic Measurements of Structural Transition and Charge Dynamics in 1 T-TiTe₂ under Pressure. *Phys Rev B* **2019**, *99* (12), 1–8. <https://doi.org/10.1103/PhysRevB.99.125105>.
- (31) Taboada-Gutiérrez, J.; Zhou, Y.; Tresguerres-Mata, A. I. F.; Lanza, C.; Martínez-Suárez, A.; Álvarez-Pérez, G.; Duan, J.; Martín, J. I.; Vélez, M.; Prieto, I.; Bercher, A.; Teyssier, J.; Errea, I.; Nikitin, A. Y.; Martín-Sánchez, J.; Kuzmenko, A. B.; Alonso-González, P. Unveiling the Mechanism of Phonon-Polariton Damping in α -MoO₃. *ACS Photonics* **2024**, *11* (9), 3570–3577. <https://doi.org/10.1021/acsphotonics.4c00485>.
- (32) Giles, A. J.; Dai, S.; Vurgaftman, I.; Hoffman, T.; Liu, S.; Lindsay, L.; Ellis, C. T.; Assefa, N.; Chatzakis, I.; Reinecke, T. L.; Tischler, J. G.; Fogler, M. M.; Edgar, J. H.; Basov, D. N.; Caldwell, J. D. Ultralow-Loss Polaritons in Isotopically Pure Boron Nitride. *Nat Mater* **2018**, *17* (2), 134–139. <https://doi.org/10.1038/nmat5047>.

- (33) Vuong, T. Q. P.; Liu, S.; Van der Lee, A.; Cuscó, R.; Artús, L.; Michel, T.; Valvin, P.; Edgar, J. H.; Cassabois, G.; Gil, B. Isotope Engineering of van Der Waals Interactions in Hexagonal Boron Nitride. *Nat Mater* **2018**, *17* (2), 152.
- (34) Liu, S.; He, R.; Xue, L.; Li, J.; Liu, B.; Edgar, J. H. Single Crystal Growth of Millimeter-Sized Monoisotopic Hexagonal Boron Nitride. *Chemistry of Materials* **2018**, *30* (18), 6222–6225. <https://doi.org/10.1021/acs.chemmater.8b02589>.
- (35) Ni, G.; McLeod, A. S.; Sun, Z.; Matson, J. R.; Lo, C. F. B.; Rhodes, D. A.; Ruta, F. L.; Moore, S. L.; Vitalone, R. A.; Cusco, R.; Artús, L.; Xiong, L.; Dean, C. R.; Hone, J. C.; Millis, A. J.; Fogler, M. M.; Edgar, J. H.; Caldwell, J. D.; Basov, D. N. Long-Lived Phonon Polaritons in Hyperbolic Materials. *Nano Lett* **2021**, *21* (13), 5767–5773. <https://doi.org/10.1021/acs.nanolett.1c01562>.
- (36) Folland, T. G.; Maß, T. W. W.; Matson, J. R.; Nolen, J. R.; Liu, S.; Watanabe, K.; Taniguchi, T.; Edgar, J. H.; Taubner, T.; Caldwell, J. D. Probing Hyperbolic Polaritons Using Infrared Attenuated Total Reflectance Micro-Spectroscopy. *MRS Commun* **2018**, *8* (4), 1418–1425. <https://doi.org/10.1557/mrc.2018.205>.
- (37) Sarkar, M.; Enders, M. T.; Shokooh-Saremi, M.; Watanabe, K.; Taniguchi, T.; Sheinfux, H. H.; Koppens, F. H. L.; Papadakis, G. T. Retrieving Optical Parameters of Emerging van Der Waals Flakes. *arXiv preprint arXiv:2305.13994* **2023**.
- (38) Segura, A.; Artús, L.; Cuscó, R.; Taniguchi, T.; Cassabois, G.; Gil, B. Natural Optical Anisotropy of H-BN: Highest Giant Birefringence in a Bulk Crystal through the Mid-Infrared to Ultraviolet Range. *Phys Rev Mater* **2018**, *2* (2). <https://doi.org/10.1103/PhysRevMaterials.2.024001>.
- (39) Esfidani, S. M. V.; Tadjer, M. J.; Folland, T. G. Lifetime and Molecular Coupling in Surface Phonon Polariton Resonators. *ACS Omega* **2024**, *9* (19), 21136–21143. <https://doi.org/10.1021/acsomega.4c01009>.
- (40) Passler, N. C.; Paarmann, A. Generalized 4×4 Matrix Formalism for Light Propagation in Anisotropic Stratified Media: Study of Surface Phonon Polaritons in Polar Dielectric Heterostructures. *Journal of the Optical Society of America B* **2017**, *34* (10), 2128–2139. <https://doi.org/10.1364/JOSAB.34.002128>.
- (41) Gubbin, C. R.; De Liberato, S. Polaritonic Quantization in Nonlocal Polar Materials. *J Chem Phys* **2022**, *156* (2), 024111. <https://doi.org/10.1063/5.0076234>.
- (42) Rogalski, A. History of Infrared Detectors A. *Opto-Electronics Review* **2012**, *20* (3), 279–308. <https://doi.org/10.2478/s11772>.
- (43) Schubert, M.; Tiwald, T. E.; Herzinger, C. M. Infrared Dielectric Anisotropy and Phonon Modes of Sapphire. *Phys Rev B* **2000**, *61* (12), 8187–8201.

Supplemental information for ‘Determining van der Waals materials’ optical and polaritonic properties using cryogenic FTIR micro-spectroscopy.’

Supplemental Section 1 - Methods

Our home built FTIR microscope uses a commercial FTIR spectrometer (Bruker Vertex 80V) with an incandescent source and an external output, which is then coupled to the microscope. Infrared light emitted by an incandescent source (SiC Glow Bar) illuminates a variable diameter pinhole (a Jacquinot Stop or J-Stop), typically set to 3mm for measurements in our system. Light passing through this pinhole is collimated by a parabolic mirror of focal length $f_{col} = 15\text{cm}$ to a beam approximately 5cm wide and passed through an interferometer and a series of mirrors into the microscope setup (not shown in Fig. 1a). A flip mirror is included at the start of the microscope to allow white light illumination for sample identification. All mirrors used in the microscope are silver to allow operation into the visible for sample identification while maintaining good mid-infrared reflection. Light from the FTIR is focused by a long focal length concave mirror (500mm), forming an image of the J-Stop at the focus, which is aligned co-inside with the back-focal length of the finite conjugate objective. This image of the J-Stop is demagnified by the ratio between the focal length of the internal collimating mirror (f_{col}) and the concave mirror (f_{con}); in our case, this gives a nominal demagnification factor of x3.3 (from f_{con}/f_{col}) and a spot approximately 10mm across at the back focal plane. We note that the aberrations inherent to using a concave mirror off-axis are relatively minimal and do not significantly influence performance. At this position, we also place a pinhole with a 0-12mm calibrated aperture to define the illumination spot on the target.

Light then travels past a D-shaped half mirror, into a reflective objective (25x – Thorlabs LMM25XF-P01), and onto the sample. The illumination spot defined by the pinhole is magnified onto the sample, which is placed inside an Oxford Instruments LHe cryostat equipped with a Cold Edge Hydra closed cycle chiller with ZnSe or KRS5 windows. The light illuminating the sample is collected by the objective and reflected by a half mirror at the back of the objective. A half-mirror ensures broadband operation and maintains a reasonable throughput and field of view (FOV), unlike conventional beamsplitter. A second motorized pinhole (ELL 15) is placed at the

objective's back focal plane after the D-shaped half mirror to define the collection area analyzed by the detector. Using two pinholes reduces the presence of scattered light in the spectrum. Motorized polarizers (ELL 14) are positioned alongside both pinholes to analyze the reflected polarization state and are equipped with KRS5 (Thorlabs WP25H-K) or ZnSe (Thorlabs WP25H-Z) polarizers. A magnetic mount mirror switches between a visible camera and an infrared detector. In the imaging position, an achromatic doublet lens focuses light onto a visible camera with a CCD area of $\frac{1}{2}$ ". We maximize the FOV to allow for easy sample identification by using a 4f configuration, enabling us to image the pinhole completely from 1mm through 12mm aperture sizes. Chromatic aberration is present between visible and IR ranges from the ZnSe window, which is compensated for in measurements by a focal shift of the cryostat between optical and infrared measurements. For infrared detection, we use a combination of mirrors and a 1" 90-degree off-axis parabolic mirror with a focal length (f_{det}) of 1", focusing on an MCT detector (IR Associates FTIR-22-0.25). The off-axis parabolic is located 30cm after the back focal length of the objective. The detector is mounted on a modular base plate so that it can be swapped out with other detectors for spectroscopy.

It is worth discussing the choice of components used in this microscope configuration and how they can be adapted for different experiments. The parameters to optimize for an FTIR microscope are light throughput, spectral resolution, and spatial resolution. To control these, one chooses the properties of the J-Stop, concave mirror, objective, detector, and collection optics. The J-Stop should be selected to maintain sufficient spectral resolution at a given wavelength for the chosen applications. In our case, we decided to achieve a spectral resolution of 0.5cm^{-1} across the full spectrum of the MCT, which is adequate for most materials' science applications. A larger J-stop can be used if a high resolution is not required, providing additional light into the microscope. A concave mirror is then chosen to fill the pinhole (accounting for the demagnification factor) and better match the detector's acceptance angle, characterized via the f-number of the components. The finite conjugate length objective lens f-number is typically low, and matching these can improve light throughput in the system ($f=0.04$ for the objective and $f=0.1$ for the concave mirror). The third choice is the objective selection, which should consider the sample sizes that need to be analyzed and the pinhole size range – here, 0-12mm. Here, we anticipate analyzing samples from $20\mu\text{m}$ - $200\mu\text{m}$, commensurate with the size of vdW flakes, choosing 50x (1mm-10mm pinhole). The final choice is the detector and collection optics. For

HgCdTe detectors, typically smaller detectors offer dramatically higher responsivity due to reduced noise in small active area detectors⁴². However, smaller detectors also require a higher magnification factor to couple to the detector, which is challenging with off-the-shelf parabolic reflectors, which have a minimum focal length of around 25mm. We use a 25mm focal length off-axis parabolic, located approximately 300mm behind the pinhole, providing a magnification of roughly 11X between the iris and the detector. We choose to use a 250 μ m x 250 μ m HgCdTe detector with a 22 μ m cutoff, which offers a good compromise between detector sensitivity and bandwidth. Sensitivity can be improved by the choice of detectors –we have implemented Si, Ge, InSb, and pyroelectric detectors in addition to the MCT to cover the far-infrared and visible between different configurations.

Isotopically pure B¹⁰ and B¹¹ enriched hBN samples were grown using the flux growth method described in the paper³⁴. Crystals were then exfoliated onto c-plane sapphire substrates and Au-coated silicon, and sufficiently large (>50 μ m x 50 μ m) flakes were identified for spectroscopy using optical techniques and atomic force microscopy (see images **Figure 2 and 3** or **Supplementary Section 2**). Sapphire substrates were chosen as they offer a low refractive index at the wavelength of the in-plane phonons, which provides a relatively flat background for dielectric function extraction. Relatively thick flakes are required for accurate dielectric function extraction, thicker than 500nm, to capture the transverse and longitudinal optical phonon energies sufficiently. Substrates with flakes were mounted onto a copper plate using silver paint, which was then screwed onto the cryostat cold head with indium foil acting as a thermal contact. A silicon diode temperature probe is mounted on the backside of the cryostat cold head to accurately monitor the sample's temperature. An Au mirror was placed next to the sample to provide an in-situ reference for all reflectance spectroscopy, and spectra were collected with a 0.5cm⁻¹ spectral resolution.

Supplemental Section 2 – Reflectance Spectra for other Flakes studied.

In this section we show full infrared reflectance spectra for a 510nm flake of h¹⁰BN and a 750nm thick flake of h¹¹BN.

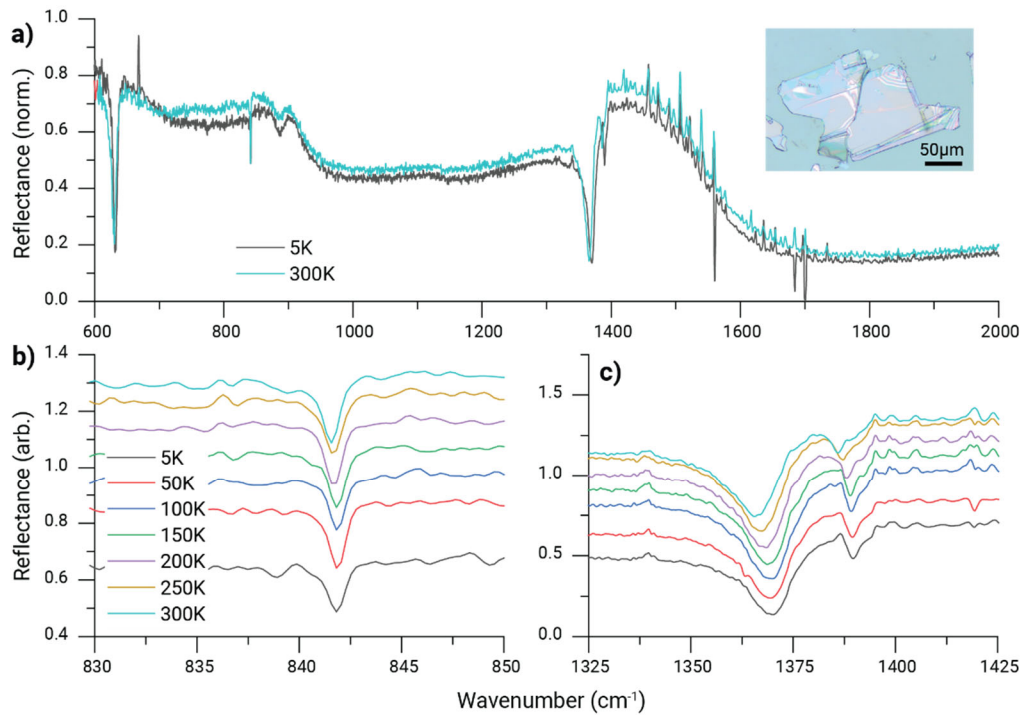


Figure S1. Temperature-dependent infrared spectra of $h^{10}\text{BN}$ isotopically enriched boron nitride on Sapphire substrates. **a)** shows broadband reflectance spectra across the mid infrared, **b)** shows detail associated with the out-of-plane phonon in $h^{10}\text{BN}$ **c)** shows detail associated with the in-plane phonon of $h^{10}\text{BN}$. Inset shows an optical microscope image of the flake.

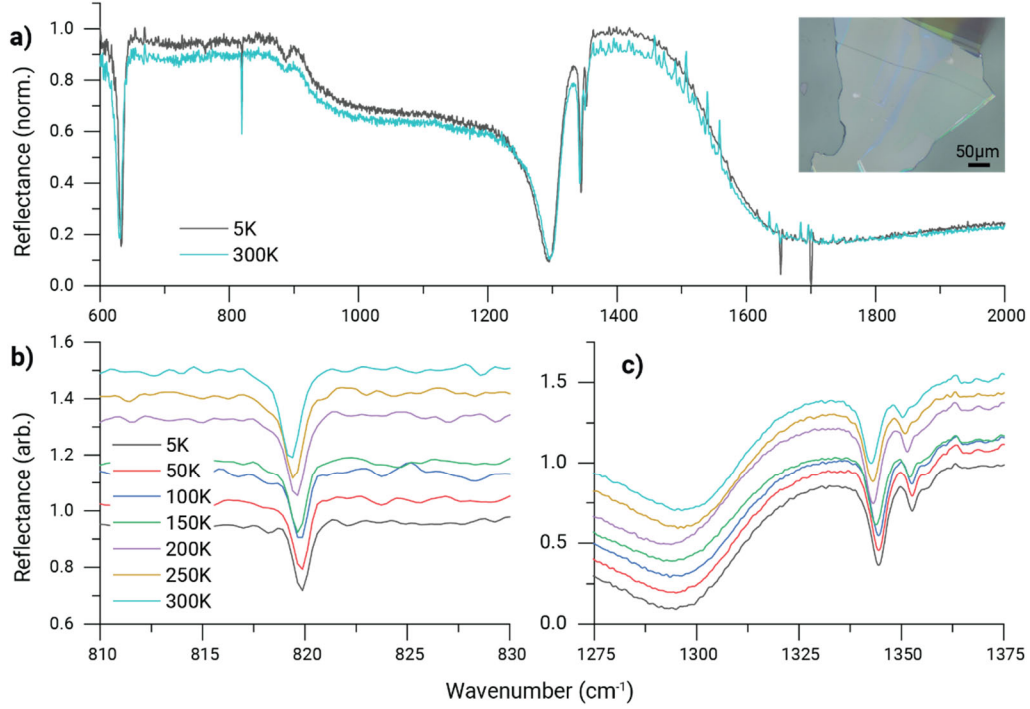


Figure S2. Temperature-dependent infrared spectra of $h^{11}\text{BN}$ isotopically enriched boron nitride on Sapphire substrates. **a)** shows broadband reflectance spectra across the mid infrared, **b)** shows detail associated with the out-of-plane phonon in $h^{11}\text{BN}$ **c)** shows detail associated with the in-plane phonon of $h^{11}\text{BN}$. Inset shows an optical microscope image of the flake.

Supplemental Section 3 – Fitting Procedure

Both vary the dielectric function parameters and construct transfer matrices that match the best fit to the reflectance data. The incident angle (20°), and polarization are set parameters, and the substrate uses room temperature literature values from ⁴³. The thickness of the flakes is determined by AFM, but is allowed to be fitted in a 5% range about the AFM measured values. The optimization first constructs the projected dielectric function for the material of interest using starting input parameters. The in-plane and out-of-plane dielectric function for hBN is modeled using the form:

$$\varepsilon = \varepsilon_\infty \frac{\omega_{LO}^2 - \omega^2 - i\Gamma\omega}{\omega_{TO}^2 - \omega^2 - i\Gamma\omega} \quad (1)$$

Where ϵ_{∞} is the high-frequency permittivity, ω_{TO} is the transverse optical phonon, ω_{LO} is the longitudinal optical phonon, and Γ is the phonon damping. Both in-plane and out-of-plane dielectric function parameters use the form above, with out-of-plane values fixed to the values from Giles³², and in-plane values fitted. The optimization then constructs the system's transfer matrices using this dielectric function and the fixed parameters for the rest of the system. The projected reflectance across the wave numbers from the experiment file is calculated and compared to the experimental reflectance using the least squares method. The above dielectric function parameters are then optimized iteratively. Error bars are constructed from the Jacobian of the fit, and the experimental and projected reflectance spectra are plotted to see the precision of the optimization. Only the in-plane dielectric function is fitted, as we can only resolve spectral features from the full Reststrahlen band in the in-plane direction. We used published data for the out-of-plane dielectric function³². The fitting includes three experimental non-idealities: angular spread, reflection scaling, and back-reflection compensation. Angular spread is achieved by averaging several spectra across the incident beam (10°). A scaling factor is included to account for the non-planarity of the sample with the microscope objective. Back reflection from the cold finger underneath the flake interfered with the spectra at higher wave numbers, as discussed in **Supplementary Section 2**. The influence of this back reflection was subtracted from the spectrum before fitting. The fit is constrained to 1000 to 2000 cm^{-1} , reducing the area that incorporates back reflections. Finally, as the measurement is most accurate where the light-matter interaction is strong about the TO phonon, this area is prioritized in the fit through error bars of 0.01 in an 80 cm^{-1} bandwidth around the TO phonon value and 0.05 outside this value.

We have experimentally found that the copper plate on which the sample is mounted can contribute significant back reflections into the sample spectrum. Figure S3 shows the sapphire substrate's experimental and simulated infrared reflection. We see significantly higher observed reflection in the transmission window of sapphire. We can subtract this back reflection from the measured spectra by transmitting a 1mm sapphire substrate to correct this. To do this, we need to assess the strength of the back reflection, which is done empirically for consistency with prior published results. We find a value of $\sim 20\%$ gives physical values the reflectance at about 2500 cm^{-1} wavenumbers. This correction's influence is compared against simulated data in Figure S3, suggesting it is a good approximation for removing back reflections. We highlight that as we can fit the back reflections from the substrate data, this can be applied to any van-der-Waals

flake. This could also be corrected by techniques such as backside roughening or mounting the sample above holes in the cryostat.

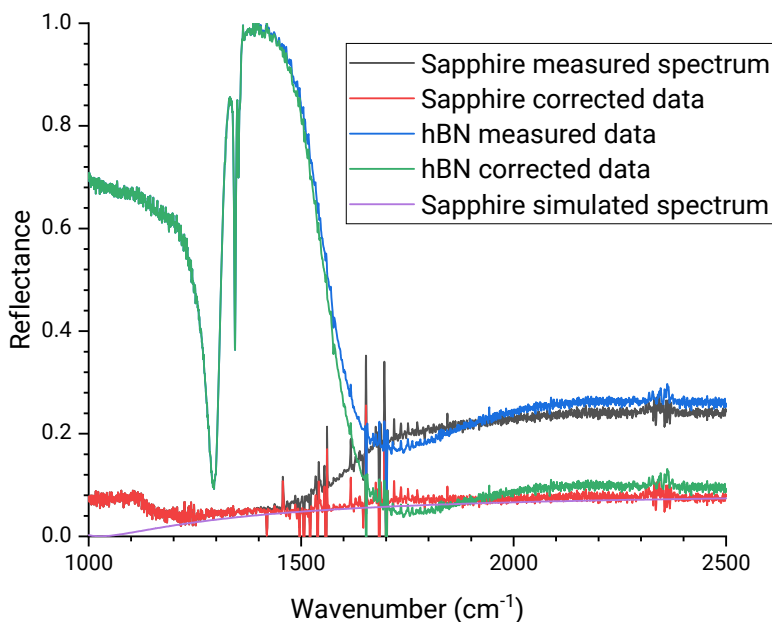


Figure S3. Role of back reflections and correction factor introduced to the spectrum.

Supplemental Section 4 – Temperature Dependent Fit Data

In this section, we present numerical fits for the temperature-dependent spectra over the fitted range for the three samples studied in this work. Figure S4 shows fit data for the 700nm h¹⁰BN flake, Figure S5 for the 510nm h¹⁰BN flake, and Figure S6 for the 750nm h¹¹BN flake. The thinner flake shows fewer FP modes than the thicker flake presented in the main text.

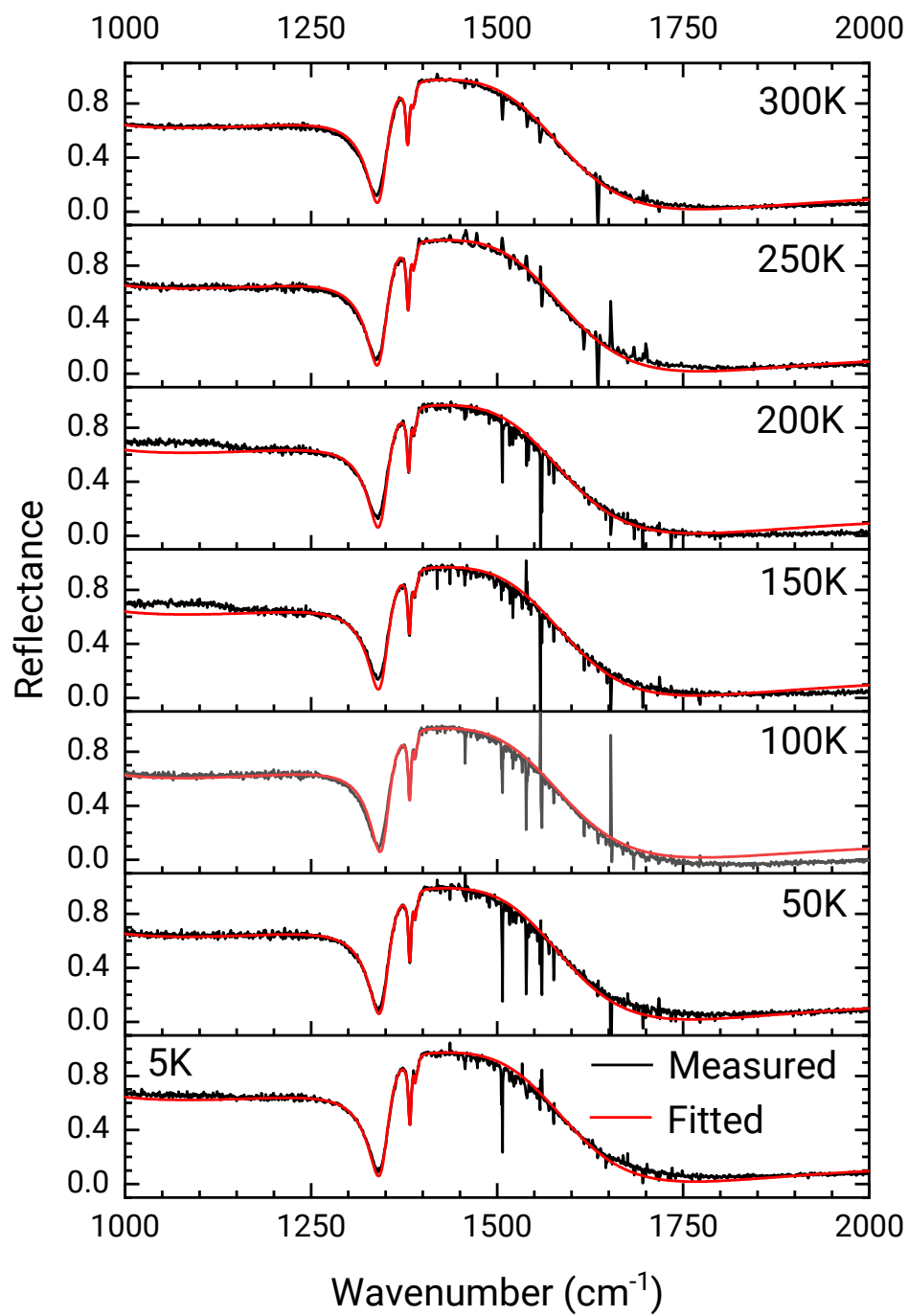


Figure S4. Temperature-dependent spectra and fit data for the 700nm h¹⁰BN flake

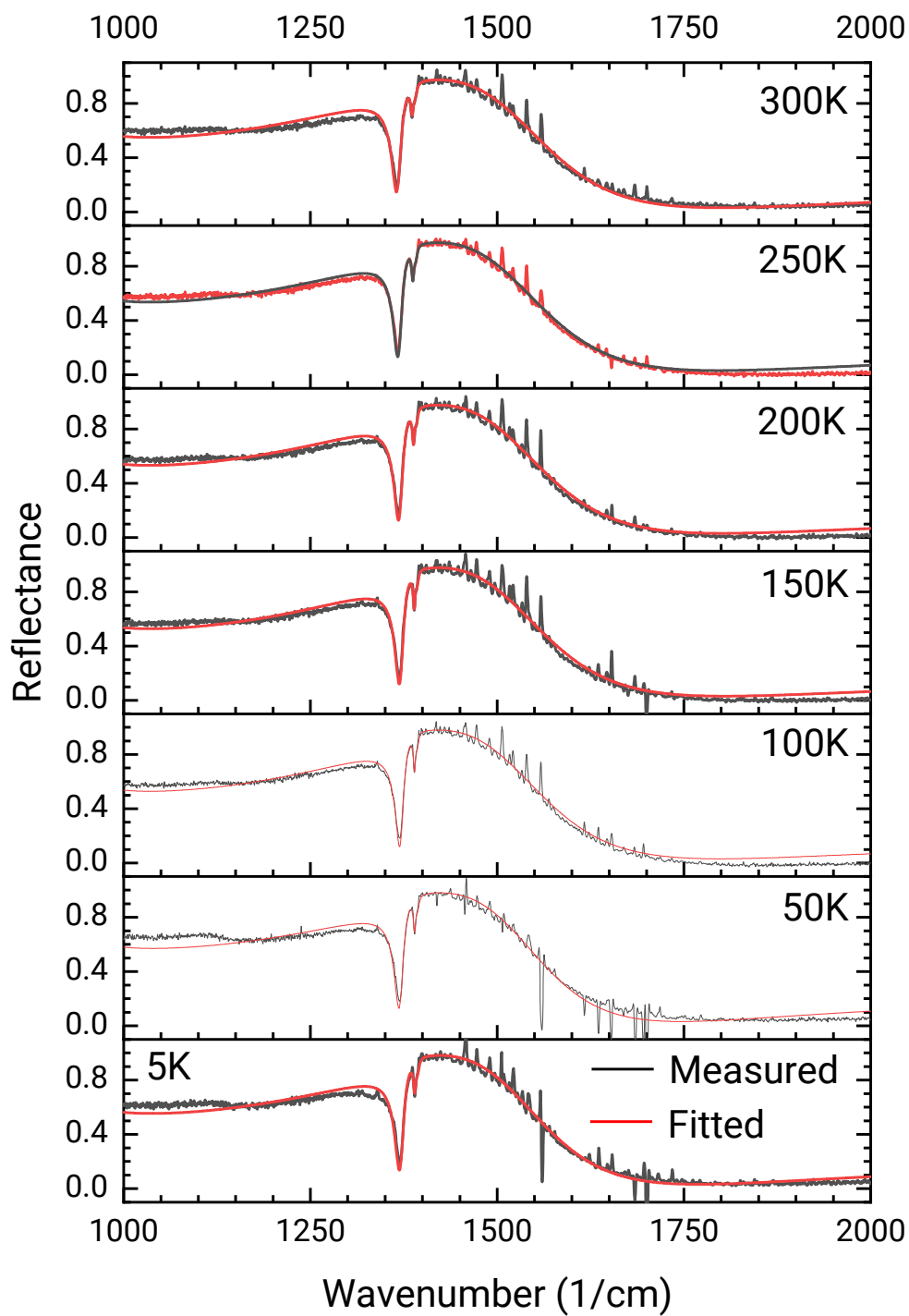


Figure S6. Temperature-dependent spectra and fit data for the 500nm h^{10} BN flake

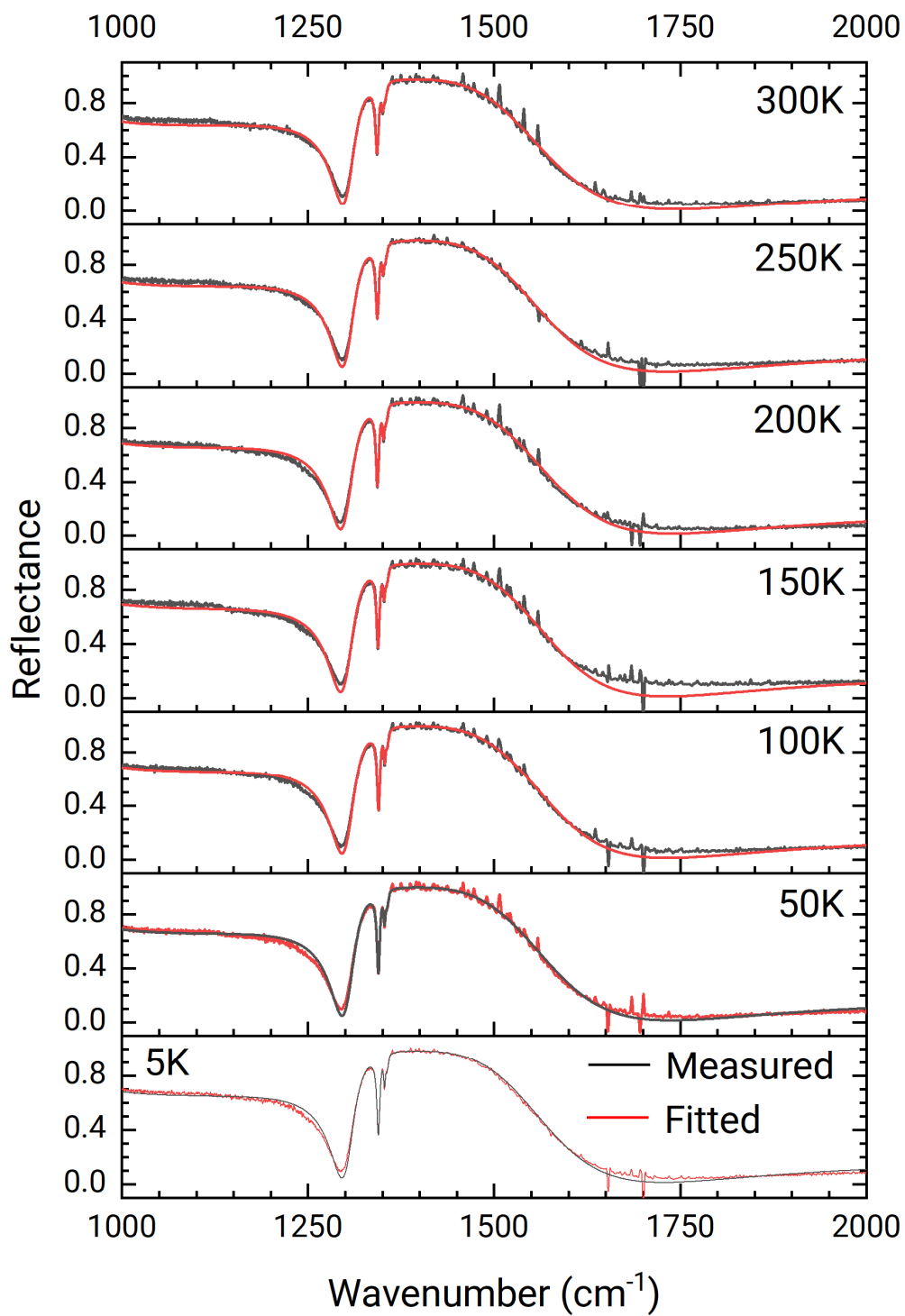


Figure S6. Temperature-dependent spectra and fit data for the 750nm h^{11} BN flake

Supplemental Section 5 – High-frequency permittivity and LO phonon data

As discussed in the main text, our fits are less consistent in the permittivity and LO phonon data. Fitted values are shown in Figure S6. The reason for this lack of sensitivity is that the LO phonon energy is most accurately determined by the zero-crossing of the dielectric function, which gives a near-zero reflectance from a bulk sample. The thin flakes do not completely absorb incident light, and the back reflections obscure this zero. This is not completely corrected through our data correction process. Further, this gives some uncertainty to the value of the high-frequency dielectric constant. However, we include the spectral range in the fit below the TO, where the dielectric function will approach ϵ_{DC} – the low-frequency permittivity. The value of ϵ_{DC} is given by the Lyddane-Sachs-Teller relations as;

$$\epsilon = \epsilon_{\infty} \frac{\omega_{LO}^2}{\omega_{TO}^2}$$

This shows that ω_{LO} and ϵ_{∞} values are coupled in the fit, explaining some systematic uncertainties in these parameters – particularly between the two thicknesses of h¹⁰BN flakes. The values we fit for the static dielectric function, also shown in **Figure S6**, show good consistency with prior work. This supports the idea that while errors exist in the fit, they are sufficiently accurate for predictive analysis of the nanophotonic properties. In particular, the results suggest that 750nm or larger flakes can give improved dielectric function estimates.

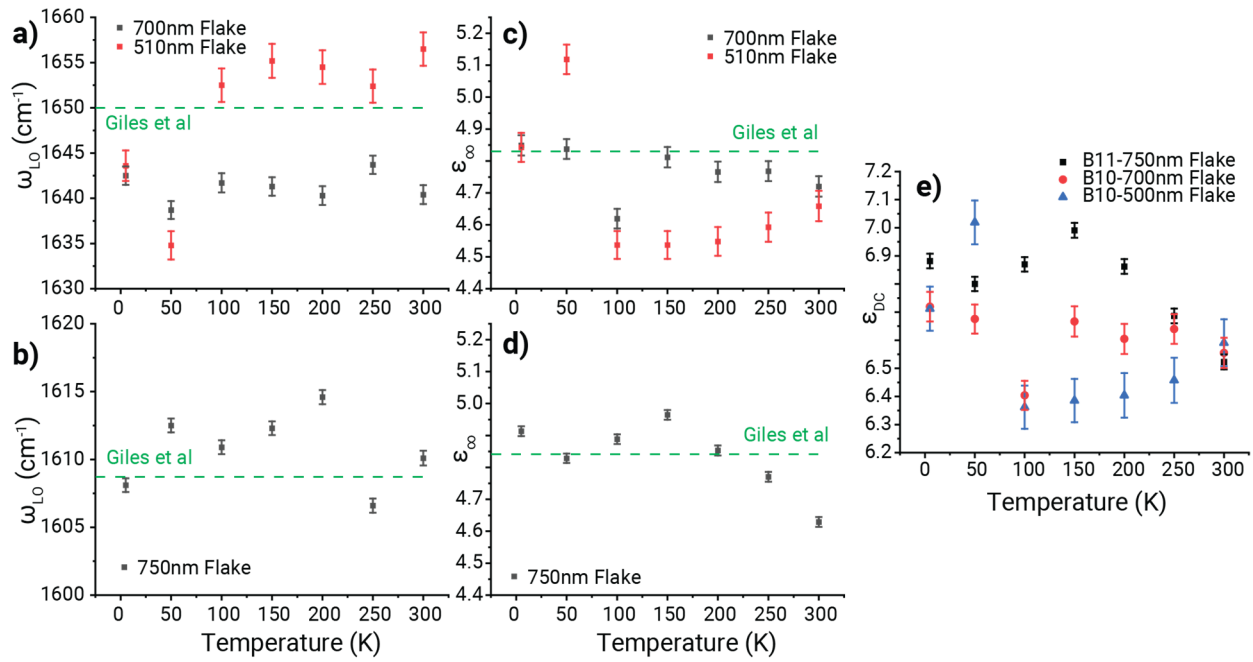


Figure S6 - ω_{LO} (a/b), ϵ_{∞} (c/d), and ϵ_{DC} (e) values for isotopically enriched B^{10} and B^{11} flakes respectively

Supplementary Section 6 – Error on fitted parameters

‘The accuracy at which FTIR spectrometry can determine a material's properties is governed by the accuracy of the FTIR spectrum measurement itself and the accuracy of the fitting procedure. The accuracy of the spectra is given by the stability of referencing for the amplitude, the instrument's spectral resolution, and the absolute calibration of the spectrometer's frequency. The accuracy of referencing is typically the weakest attribute of infrared reflection spectroscopy, with deviations that can be as much as 10%. This is easy to account for in fitting the experimental spectra (through a normalization) and does not influence our ability to observe spectral peaks. The resolution of the FTIR is more subtle. The spectral resolution of the FTIR is determined by the path length of the moving mirror and the maximum full-width half maximum ‘peak’ which can be resolved. However, the position of a peak that is wider than this limit can be determined at an accuracy below the resolution of the spectrometer by zero-filling the interferogram before it is Fourier transformed to generate a spectrum. This is a standard data processing step on FTIR spectrometers; see reference 19. This artificially interpolates the data and allows one to determine the center of a peak with significantly higher precision, limited by the absolute accuracy of the FTIR. The Fabry Perot mode peak positions can be determined by a Lorentz fit to the spectrum, with errors given purely by the deviations between the Lorentz fit and the experimental data, as is reported in the main text. The calibration laser used to track the position of the moving mirror gives absolute accuracy. This can be checked by using high-resolution measurements of molecular absorption lines using reference cells but can be approximately validated by measuring the 667.6cm^{-1} CO_2 absorption band, which is measured to within 0.1cm^{-1} for our spectra at an instrument resolution of 0.5cm^{-1} with 64x points of zero-filling interpolation, matching the accuracy of reported fits.

Whilst these general principles determine the accuracy of measuring features in FTIR spectra, they do not necessarily relate to the dielectric function fit. The nonlinear least squares algorithm used to fit the data will output an error calculated based on the sensitivity of the fit to the numerical data presented. However, this can hide systematic errors in fitting, as it will depend on the data density and noise in the spectrum. An excellent example is the measurements presented in Figure 4c, where the error bar is approximately 0.1cm^{-1} for all the points, but two flakes give different results well outside this margin of error. A better approach to estimating the errors is by

calculating the standard deviation between the temperature-dependent fits, which allows us to calculate the error in determining both the frequency and damping rate of the TO phonon and damping at 0.9cm^{-1} and 0.47cm^{-1} , respectively. Both are close to the spectral resolution of the FTIR, suggesting that this might provide a rough approximation of systematic errors in the fitting. Another approach for calculating error can be used when no significant change in a parameter is observed as a function of temperature. In this case, systematic errors give a random spread to the data, and the error can be estimated directly from the standard deviation of the parameter as a function of temperature.'

Supplemental Section 7 – Validation via reflectance of flakes on Au substrate.

In this section, we show that our fitted dielectric function can be used to adequately describe the optical properties of hBN, as shown in Figure S7. We can correctly predict the frequencies and linewidths of the infrared-measured FP modes, as well as the associated temperature tuning.

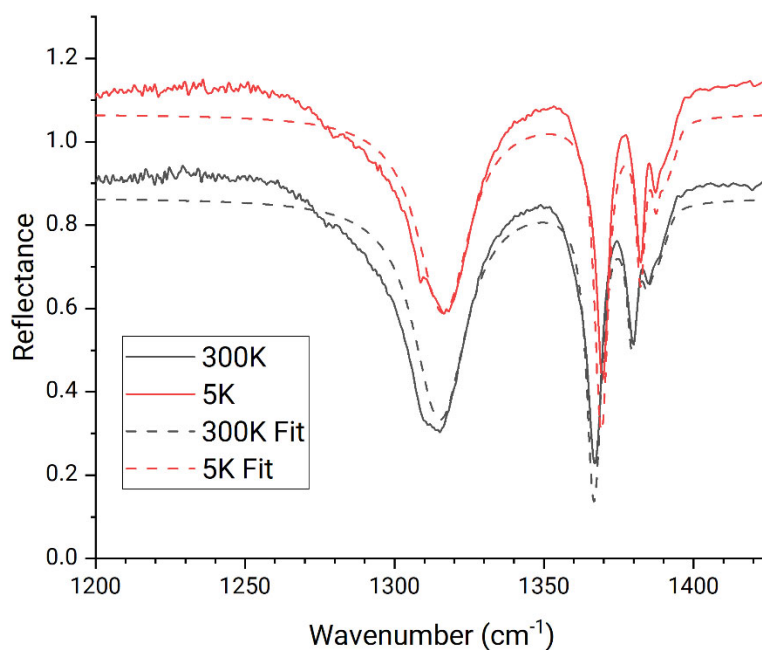


Figure S7 – Validation of dielectric function fit using 1220nm thick B10 hBN data.

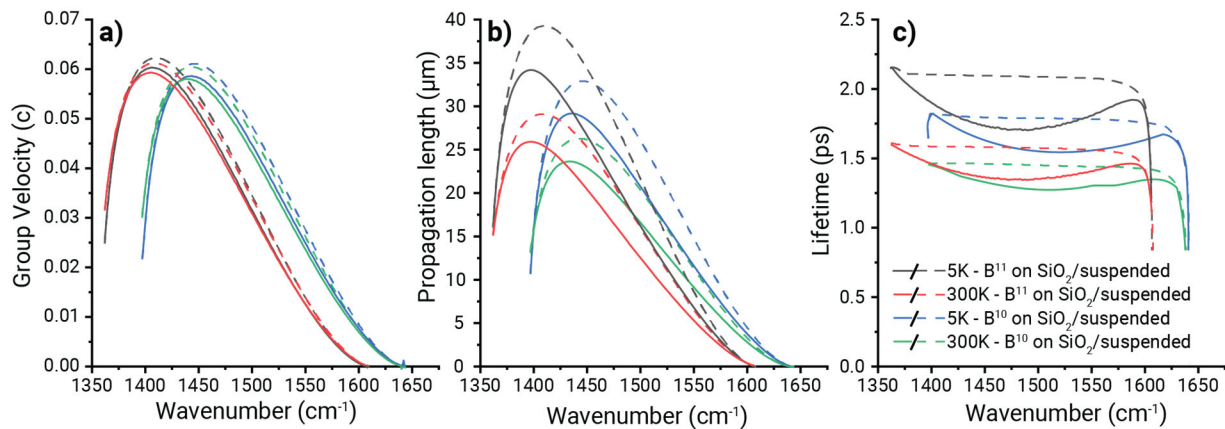


Figure S8, group velocity, propagation length and lifetime for polaritons in a 710nm thick flake of hBN of different isotopic content and on different substrates.